Refractory inclusions in the unique carbonaceous chondrite Acfer 094

Steven B. SIMON[1*] and Lawrence GROSSMAN[1,2]

[1]Department of the Geophysical Sciences, 5734 S. Ellis Ave., The University of Chicago, Chicago, Illinois 60637, USA
[2]The Enrico Fermi Institute, 5640 S. Ellis Ave., The University of Chicago, Chicago, Illinois 60637, USA
[*]Corresponding author. E-mail: sbs8@uchicago.edu

Abstract–Acfer 094 is an unshocked, nearly unaltered carbonaceous chondrite with an unusual suite of refractory inclusions. The refractory inclusions in a newly prepared thin section and a small aliquot of disaggregated material were studied to compare the population with previous work, and to report new or unusual inclusion types. A total of 289 Ca-, Al-rich inclusions in the thin section and 67 among the disaggregated material, having a total of 31 different mineral assemblages, were found. Inclusions are largely free of secondary alteration products, and are typically ≤200 μm across. The most common are gehlenitic melilite + spinel ± perovskite, spinel + perovskite, and spinel with a thin, silicate rim, typically melilite ± diopside. Such rims and (thicker) mantles are very common among Acfer 094 inclusions, and they exhibit a variety of zoning patterns with respect to åkermanite and FeO contents. In the thin section, about 13% of the inclusions contain hibonite and approximately 5% are grossite-bearing; in the disaggregated material, the percentages are 14 and 9, respectively, comparable to previous work. Among the unusual inclusions are a fine-grained, porous, Ti-rich hibonite + spinel + perovskite + melilite inclusion with a compact, coarse, Ti-poor hibonite + spinel + melilite clast; two inclusions in which hibonite has reacted to form grossite; two inclusions with FeO-rich spinel; and a small object consisting of fassaite enclosing euhedral spinel, the first fragment of a Type B inclusion reported from Acfer 094. Inclusions similar to those found in CM or CV chondrites are rare; Acfer 094 contains a distinctive population of inclusions. The population, dominated by small, melilite-bearing inclusions, is most similar to that of CO chondrites. A distinguishing feature is that in Acfer 094, almost every phase in almost every refractory inclusion contains 0.5–1.5 wt% FeO. A lack of diffusion gradients and the pristinity of the matrix imply that the inclusions experienced prolonged exposure to FeO-bearing fluid prior to accretion into the Acfer 094 parent body. There are no known nebular conditions under which the refractory phases found in the present samples could acquire FeO enrichments to the observed levels. The most likely setting is therefore in an earlier, FeO-rich parent body. The inclusions were ejected from this parent body, mixed with typical CAIs, chondrules, amoeboid olivine aggregates, and amorphous material, and incorporated into the Acfer 094 parent body.

INTRODUCTION

Acfer 094 is a unique type 3 carbonaceous chondrite. It was first described as having trace element characteristics of CM chondrites and mineralogical features of CO chondrites (Bischoff et al. 1991), and it has defied classification ever since. As pointed out by Newton et al. (1995), its O isotopic composition is not consistent with membership in either of those groups, and its C and N isotopic compositions do not match any group. Its matrix is an unequilibrated assemblage consisting of nodules of amorphous silicates enclosing crystalline silicates and sulfides (Greshake 1997; Keller et al. 2009). Studies show that the amorphous silicates have excess oxygen, consistent with hydration, but little phyllosilicate formation occurred (Greshake 1997; Keller et al. 2009). This shows that hydration was limited, and the presence of amorphous silicates indicates that Acfer

094 experienced minimal alteration on the parent body. Presolar silicates are easily destroyed by aqueous alteration, and are more abundant in Acfer 094 than in almost all other meteorites (Vollmer et al. 2009), further indicating a highly pristine nature. It is also essentially unshocked (Newton et al. 1995), and clastic material is very rare in the matrix (Greshake 1997; Bland et al. 2007). Much work has been done on Acfer 094 because it is a unique, pristine carbonaceous chondrite.

Work that has been done on the refractory inclusion population shows that it also is not readily classified in comparison to those of known groups, contributing to the uniqueness of Acfer 094. Weber (1995) showed that the refractory inclusions are largely unaltered and are most similar to Ca-, Al-rich inclusions (CAIs) from CO and CR chondrites. Krot et al. (2004a) studied three thin sections of Acfer 094 and concluded that, although the CAIs in it are most similar to those from CO chondrites, they are a mineralogically distinct population. Chondrites can be heterogeneous, as most of them, including Acfer 094, are breccias. The CAI population in this unique meteorite should be characterized as thoroughly as possible to search for heretofore undiscovered CAI types, and to learn as much as possible from them. Therefore, when the U.S. National Museum of Natural History acquired a previously unstudied sample of Acfer 094, a polished thin section was requested to: document the refractory inclusion population in it; compare the population with previous descriptions of Acfer 094 CAIs; and to report any new or unusual inclusions. Objects from a small aliquot (less than approximately 0.1 g) of Acfer 094 that had previously been disaggregated at Washington University in a search for presolar grains, were also hand-picked, mounted, and polished. Preliminary results of this study were given by Simon and Grossman (2009).

ANALYTICAL METHODS

The approximately 50 mm^2 thin section (USNM 7233-1) was searched for refractory inclusions by simultaneously collecting backscattered electron images and Al Kα X-ray maps at 15 kV with a JEOL JSM-5800 LV scanning electron microscope (SEM) equipped with an Oxford/Link ISIS-300 energy-dispersive X-ray analysis system (EDS). Phases in Al-rich objects found this way were identified using EDS. Hand-picked particles were mounted in epoxy, polished, carbon-coated, and examined with the SEM. Quantitative wavelength-dispersive analyses were collected with a fully automated Cameca SX-50 electron microprobe operated at 15 kV. Data were reduced using the modified ZAF correction procedure PAP (Pouchou and Pichoir 1984).

RESULTS

CAI Population in Thin Section

A total of 289 refractory inclusions and 22 amoeboid olivine aggregates (AOAs) were found in the thin section. These objects account for approximately 0.5% of the area of the thin section. Al-rich chondrules were observed, but are not included in this study because they are not refractory inclusions. Most of the Al-rich objects are partially to completely enclosed in one or more rim layers of melilite, aluminous diopside, anorthite, or forsterite. Some have mantles of melilite with rims of Al-diopside. A "rim" is defined herein as a thin, outer layer of a phase not present in the interior, such as the anorthite and diopside layers shown in Fig. 1a. An enclosing layer of melilite is termed a "mantle" if it is relatively thick compared with the diameter of the inclusion, and if melilite is also present in the interior of the inclusion (e.g., Fig. 1b). Refractory inclusions in Acfer 094 are mostly fragments, and are typically smaller and finer-grained than those found in CV3 chondrites. Even including the rims and mantles, they are typically < 200 μm across. Many inclusions have melilite either as a major interior phase, a mantle, or a rim. The melilite is largely unaltered. Approximately 13% of the inclusions found contain hibonite, and 5% contain grossite. In comparison, approximately 10% of the inclusions found by Krot et al. (2004a) are hibonite-bearing, and approximately 10% are grossite-bearing.

The CAIs in the present section have 27 different mineral assemblages (not including rim phases), listed in Table 1 in order of abundance. Representative examples of some of the common inclusion types are shown in Fig. 1. For the purposes of classification, pyroxene is identified as either Ti-rich (Tpyx), with > 3 wt% Ti as TiO$_2$ (TiO$_2^{tot}$), or Ti-poor (diopside, or "Diop"). The most common inclusions consist of gehlenitic melilite either enclosing fine spinel $\pm$ perovskite poikilitically (Fig. 1a) or as a mantle in nodular inclusions (Fig. 1b). The next most abundant are spinel-perovskite inclusions (Fig. 1c). In these, anhedral perovskite grains are enclosed in spinel, and this assemblage is typically enclosed in a silicate rim, usually melilite $\pm$ diopside. Spinel grains with silicate rims are the third most abundant type of Al-rich object, followed by fine intergrowths of anhedral anorthite and pyroxene (Fig. 1d) and spinel-pyroxene inclusions (Fig. 1e). The one shown in Fig. 1e is a fragment of a larger, probably convoluted inclusion reminiscent of the melilite-free, spinel-, pyroxene-rich "OC" inclusion type first recognized among Murchison inclusions (MacPherson et al. 1983).
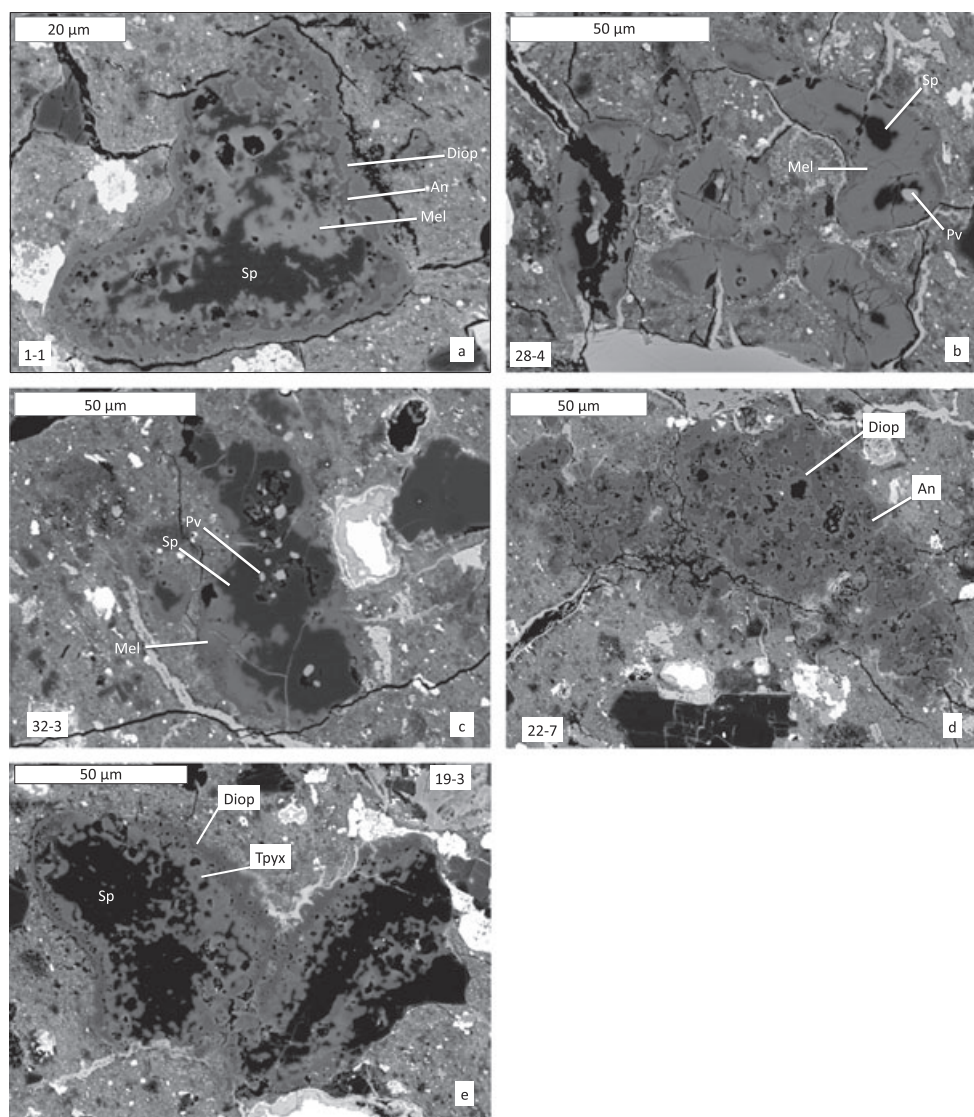
Fig. 1. Backscattered electron images of the most abundant inclusion types. a) Inclusion 1-1, a spinel-melilite inclusion with spinel poikilitically enclosed in melilite, with rim layers of anorthite and diopside. b) Inclusion 28-4, a nodular spinel-melilite-perovskite inclusion. c) Inclusion 32-3, a spinel-perovskite inclusion, melilite rim. d) Inclusion 22-7, a fine intergrowth of anorthite and diopside. e) Inclusion 19-3, a spinel-pyroxene inclusion. An = anorthite; Diop = diopside; Mel = melilite; Pv = perovskite; Sp = spinel; Tpyx = Ti-bearing pyroxene.

CAIs in the Disaggregated Material

A total of 67 CAIs and six AOAs were found in the (>1 μm) disaggregated material. Most occur within incompletely disaggregated meteorite fragments and were found by Al-mapping. The proportion of Sp + Mel ± Pv inclusions (19.4%) is about the same as that in thin section (22.5%); Sp + Pv inclusions (10.4%) are less abundant and An + Pyx inclusions (20.9%) are more abundant than in thin section (Table 1). Four inclusions, all hibonite-bearing, have mineral assemblages that were not found in the thin section. They are hibonite + grossite + spinel (two

samples), corundum + hibonite + grossite + spinel, and hibonite + kushiroite (CaTs-rich pyroxene; Kimura et al. 2009). The latter is probably a fragment of a hibonite-aluminous pyroxene spherule like those previously seen in Acfer 094 (Krot et al. 2004a) and other carbonaceous chondrites (Simon et al. 1998).

Hibonite- and Grossite-Bearing Inclusions

Most commonly, hibonite occurs as laths enclosed in spinel and perovskite, with the assemblage enclosed in melilite. Unlike those in CM chondrites, hibonite-spinel

Table 1. Mineralogy of refractory inclusions found in thin section USNM 7233-1.

Mineralogy	No. of objects	% of objects
Sp + Mel ± Pv	65	22.5
Sp + Pv	47	16.3
Sp	28	9.7
An + Pyx	28	9.7
Hib + Sp + Mel ± Pv	20	7.0
Sp + An + Diop	17	5.9
Sp + Pyx	11	3.8
Sp + An	10	3.5
Sp + Mel + Tpyx	8	2.8
Hib + Gro + Sp + Mel ± Pv	8	2.8
Mel + An + Sp	8	2.8
Mel + An + Pyx	7	2.4
Hib ± Sp ± Pv	6	2.1
Gro + Sp + Mel + Pv	5	1.7
Mel + An	5	1.7
Sp + Mel + Diop + An	2	0.7
Mel + Pv + An	2	0.7
Gro + Pv + Sp	2	0.7
Tpyx + Diop + pv	2	0.7
Cor + Hib	1	0.3
Hib + Sp + Fo	1	0.3
Hib + Mel	1	0.3
Sp + Tpyx + An	1	0.3
Sp + Mel + Diop + Pv	1	0.3
Sp + Mel + Fo + FeS + Diop	1	0.3
Mel + Pv	1	0.3
Mel + Diop + Fo	1	0.3

Sp = spinel; Mel = melilite; Pv = perovskite; An = anorthite; Pyx = pyroxene; Hib = hibonite; Diop = diopside; Tpyx = Ti-bearing pyroxene; Gro = grossite; Cor = corundum; Fo = forsterite. "Pyx" indicates that some members of the group contain diopside and others contain Tpyx.
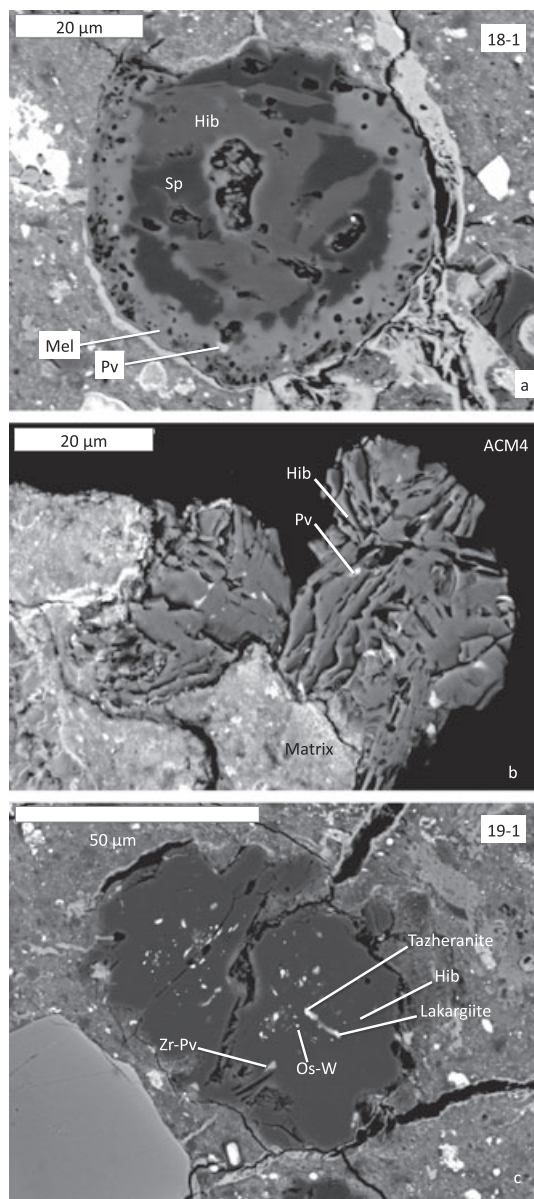

Fig. 2. Backscattered electron images of hibonite occurrences in Acfer 094. a) Inclusion 18-1, a hibonite-spinel-perovskite spherule with a melilite rim. b) Inclusion ACM4, an aggregate of hibonite laths with interstitial perovskite. c) Inclusion 19-1, a relatively large hibonite plate with fine inclusions of Zr-bearing perovskite and other Zr-rich phases. Hib = hibonite; other abbreviations as in previous figure.

inclusions in Acfer 094 commonly have melilite rims (e.g., Fig. 2a). On the other hand, like their counterparts in CMs (e.g., MacPherson et al. 1983), many Acfer hibonite-bearing inclusions have cavities. Hibonite also occurs as a cluster of laths with interstitial perovskite (Fig. 2b) and in grossite-bearing inclusions (see below). Occurrences in thin section include a small (25 μm) inclusion fragment consisting of hibonite and corundum and a relatively coarse, platy hibonite crystal (Fig. 2c) with fine inclusions of tazheranite (cubic zirconia), lakargiite (CaZrO$_3$), Zr-bearing perovskite, and Os-W nuggets (Ma 2011).

A typical grossite-bearing inclusion is shown in Fig. 3a. It has a core of massive, anhedral grossite enclosing fine perovskite grains, and a melilite rim. The grossite is partially separated from the melilite by a discontinuous layer of spinel. Grossite and hibonite occur together in inclusions that display a wide range of textures. In some cases, the two phases are not in contact with each other, typically because hibonite and grossite

are enclosed in, and therefore separated by, spinel. They occur in different parts of a relatively large, porous inclusion, 59-1 (Fig. 3b), which consists of anhedral grains of grossite, hibonite, and spinel, all with melilite rims. The inclusion has anorthite and diopside rim layers along one edge. In inclusion L5-1 (Fig. 3c), anhedral grossite occurs in interstices between hibonite laths. Some of the hibonite has reacted, presumably
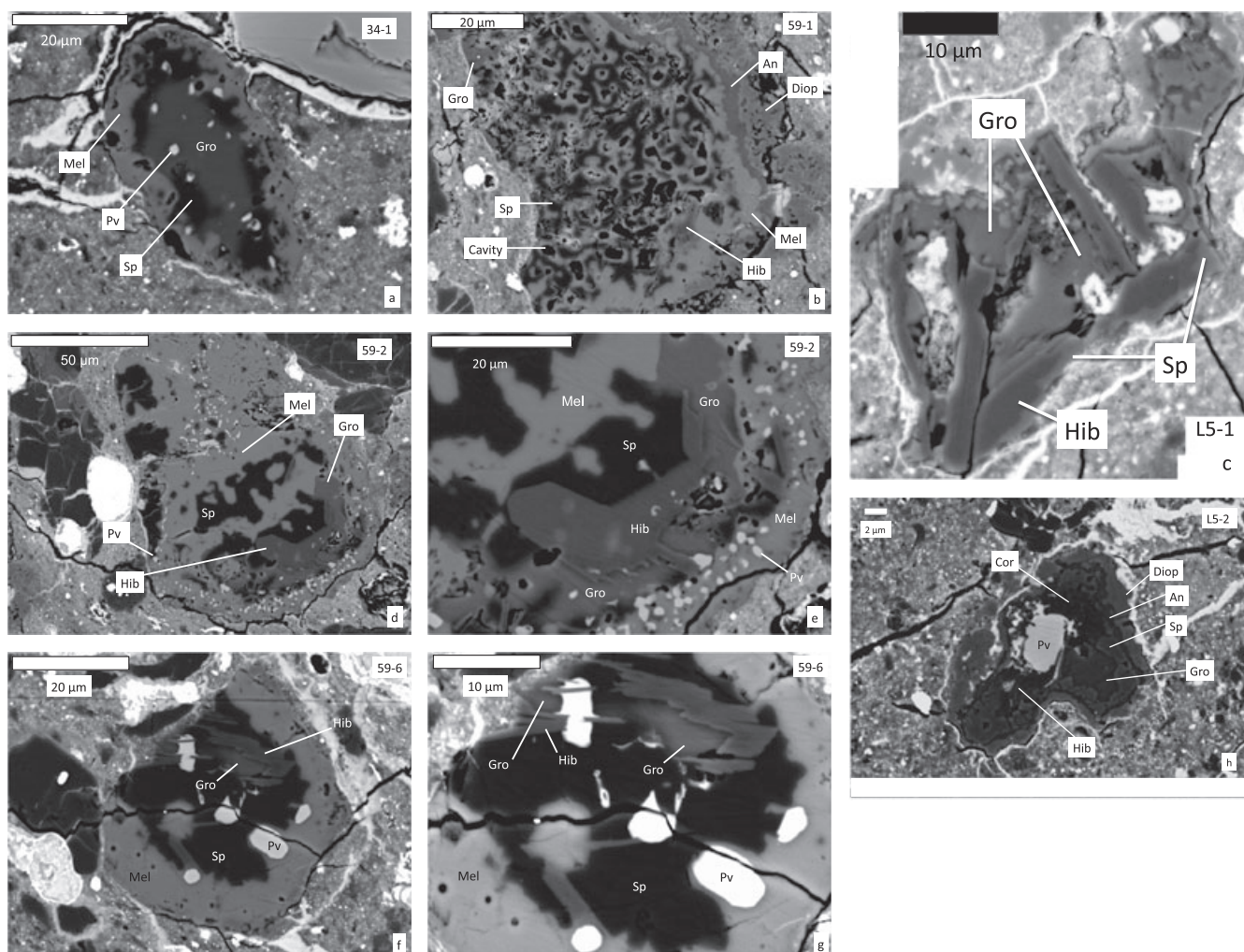
Fig. 3. Backscattered electron images of grossite-bearing inclusions in Acfer 094. a) Inclusion 34-1, a typical occurrence with a massive grossite-perovskite core, a discontinuous layer of spinel, and a melilite rim. b) Inclusion 59-1, a porous inclusion with anhedral grossite, hibonite, and spinel. Individual grains have melilite rims. c) Inclusion L5-1, consisting of hibonite laths with interstitial grossite and alteration products. Outer margins of the hibonite laths have been converted to spinel. d) Inclusion 59-2. Note the straight, crystallographically controlled hibonite-spinel contacts and the corroded contacts between melilite and spinel and between hibonite and grossite. e) Inclusion 59-2, higher magnification view of contacts between hibonite, spinel and grossite. f) Inclusion 59-6, a spherule with a core of hibonite, grossite, perovskite, and spinel enclosed in melilite. As in 59-2, spinel-melilite and hibonite-grossite contacts are irregular, whereas hibonite-spinel contacts are straight. g) Inclusion 59-6, higher magnification view. h) Inclusion L5-2, consisting of a grossite-rich interior with a large perovskite grain and smaller, sparse corundum and hibonite grains, enclosed in a layer of FeO-rich spinel. Image courtesy of C. Ma, Caltech. Cor = corundum; Gro = grossite; other abbreviations as in previous figures.

with nebular gas, to form spinel. In contrast, in two, more compact hibonite-grossite-spinel-perovskite-melilite inclusions, 59-2 (Figs. 3d and 3e) and 59-6 (Figs. 3f and 3g), the contacts between hibonite and spinel are straight and smooth whereas those between hibonite and grossite are irregular. Inclusion 59-2 is a rounded object with anhedral spinel and perovskite enclosed in melilite, with hibonite, minor grossite, and cavities concentrated toward one end. Inclusion 59-6 is also rounded, with a core of perovskite, grossite, hibonite, and melilite enclosed in spinel, all enclosed in a mantle of melilite +

perovskite. In both of these inclusions, contacts between spinel and melilite are rounded and embayed (Figs. 3e and 3g). Another interesting inclusion is L5-2 (Fig. 3h). It is very small, just approximately 20 × 10 μm. The interior of the inclusion consists mainly of grossite and perovskite, with a few approximately μm-sized grains of corundum (identification confirmed using electron backscattered diffraction analysis). The grossite-rich area is enclosed in a chain of subhedral spinel grains. The outer edges of the spinel grains are smoothly aligned with each other, unlike the inward-facing crystal faces,
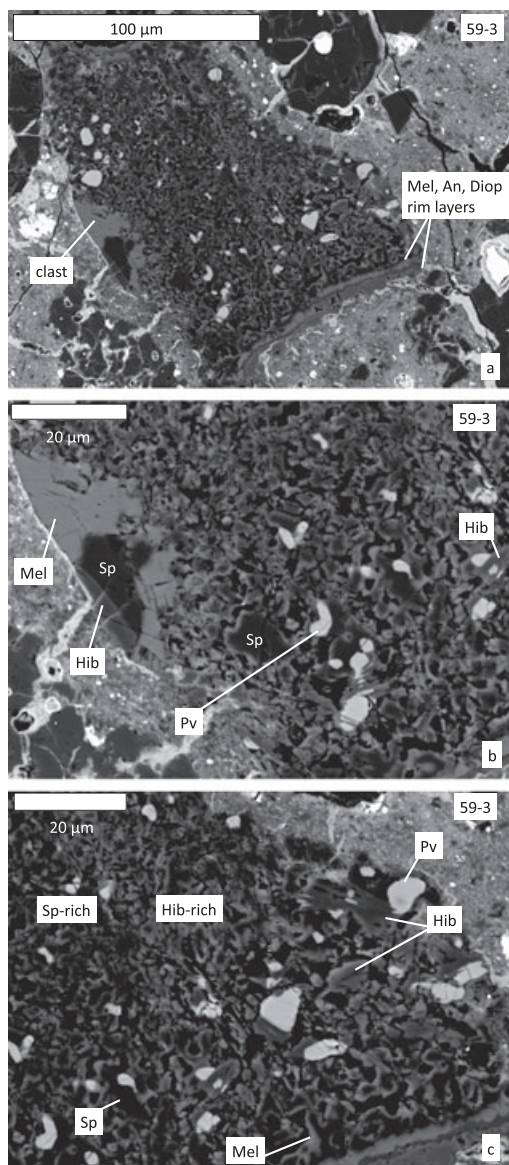
Fig. 4. Backscattered electron images of compound inclusion 59-3. a) View of the entire inclusion fragment, showing the coarse-grained clast, fine-grained host, and rim layers. b) View of clast and adjacent spinel-rich host. Note the arcuate contact between clast and host, intergrowth of phases along it, and melilite (light) rims on spinel grains. c) View of hibonite-rich (right) and spinel-rich (left) parts of host. Abbreviations as in previous figures.

which jut into the adjacent grossite. To the exterior of the spinel are a thin layer of anorthite and thicker layer of aluminous diopside.

Other Notable Inclusions

Compound Inclusion

One inclusion fragment, 59-3 (Fig. 4), has a fairly complex texture. It has a relatively coarse-grained, compact
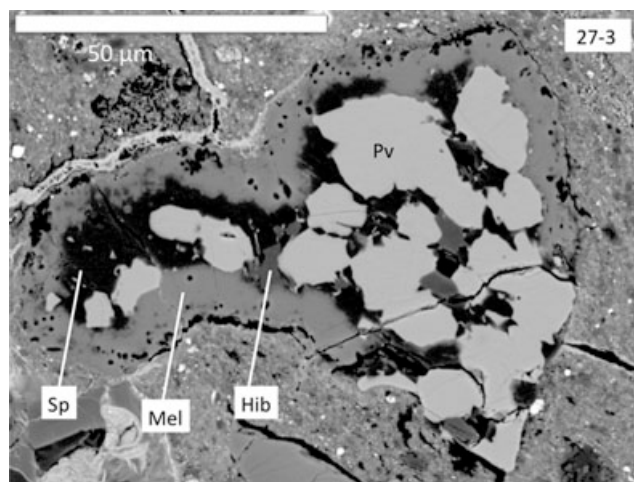

Fig. 5. Backscattered electron image of inclusion 27-3, a perovskite-rich inclusion with interstitial hibonite and spinel, enclosed in a melilite rim. Abbreviations as in previous figures.

clast in a finer-grained, porous host (Figs. 4a and 4b). The clast consists of hibonite and spinel in a melilite ($Åk_{0–5}$) mantle. The host consists of anhedral to subhedral hibonite, perovskite, and spinel. The contact between the clast and host is curved on a large scale (Fig. 4a) and jagged on a fine scale (Fig. 4b). Within approximately 50 μm of the clast, the host is quite spinel-rich, unlike the other side of the inclusion, which is hibonite-rich. Portions of both regions are shown in Fig. 4c, with the spinel-rich region to the left and the hibonite-rich region to the right. In both regions, many grains have thin rinds of melilite. The inclusion also has a sequence of rim layers, from innermost to outermost, of melilite, anorthite, and diopside along two of its edges.

Perovskite-Rich Inclusion

One inclusion, 27-3 (Fig. 5), consists of a typical mineral assemblage of hibonite, spinel, and perovskite with a melilite rim. Unlike most other Acfer 094 inclusions, in which perovskite occurs as tiny blebs, the perovskite in this inclusion is relatively coarse, dominantly occurring as grains up to approximately 20 μm across, in addition to tiny blebs, with interstitial hibonite. Spinel occurs interstitially, and partially encloses some perovskite grains. Perovskite composes 44 vol% of the inclusion. Krot et al. (2004a) also reported a very perovskite-rich inclusion from Acfer 094.

Type B Inclusion Fragment

One small (30 × 30 μm), unrimmed fragment, shown in Fig. 6, is best described as a fragment of a Type B inclusion, the first one reported from Acfer 094. It consists of euhedral spinel partially enclosed in Ti-bearing pyroxene. Unlike this inclusion, most inclusions
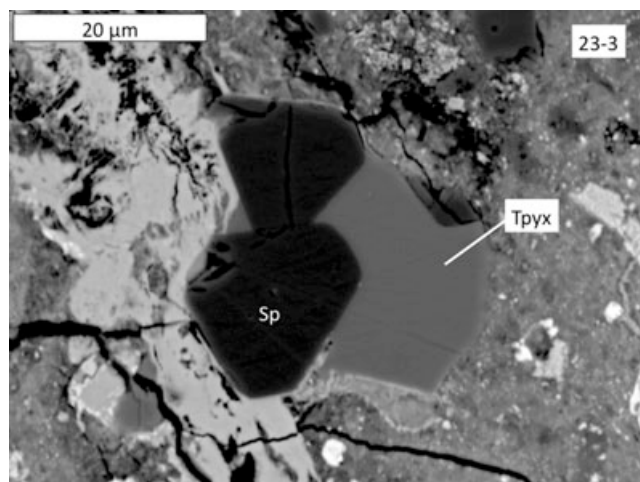
Fig. 6. Backscattered electron image of inclusion 23-3, probably a fragment of a Type B coarse-grained refractory inclusion. The unrimmed fragment consists of euhedral spinel partially enclosed in fassaite. Abbreviations as in previous figures.

in Acfer 094 have rims, Ti-poor pyroxene (if any) and finer-grained, anhedral spinel.

Amoeboid Olivine Aggregates

Amoeboid olivine aggregates found in this study are like some of those shown in Krot et al. (2004b). Those in the present study are dominated by fine-grained, forsteritic olivine, anorthite, and diopside, with minor amounts of spinel. There are two main textural types. One (Fig. 7a) has olivine mainly occurring along the outer edges of the inclusion, enclosing fine intergrowths of anorthite and aluminous diopside. The other common type (Fig. 7b) has an unzoned intergrowth of olivine, anorthite, and diopside ± spinel. These two textures can be considered endmembers of a continuum, as some samples have intermediate textures, such as those with olivine mainly at the edges but also in the interior.

Rim Layers on Inclusions

Approximately half of the inclusions have a partial to complete rim layer, mantle, or sequence of layers. Of these, approximately 60% have rims consisting of only aluminous diopside, approximately 30% have only melilite, and approximately 10% have both. Those with both commonly have relatively thick melilite and thin Al-diopside rims, and some inclusions have sequences of layers, typically melilite, anorthite, and diopside. Where both melilite and diopside rims are present, the latter is the outermost layer. The melilite layers in both rims and mantles occur as continuous bands, with no indications of grain boundaries visible either in the SEM or optically. The rims on Acfer inclusions clearly differ
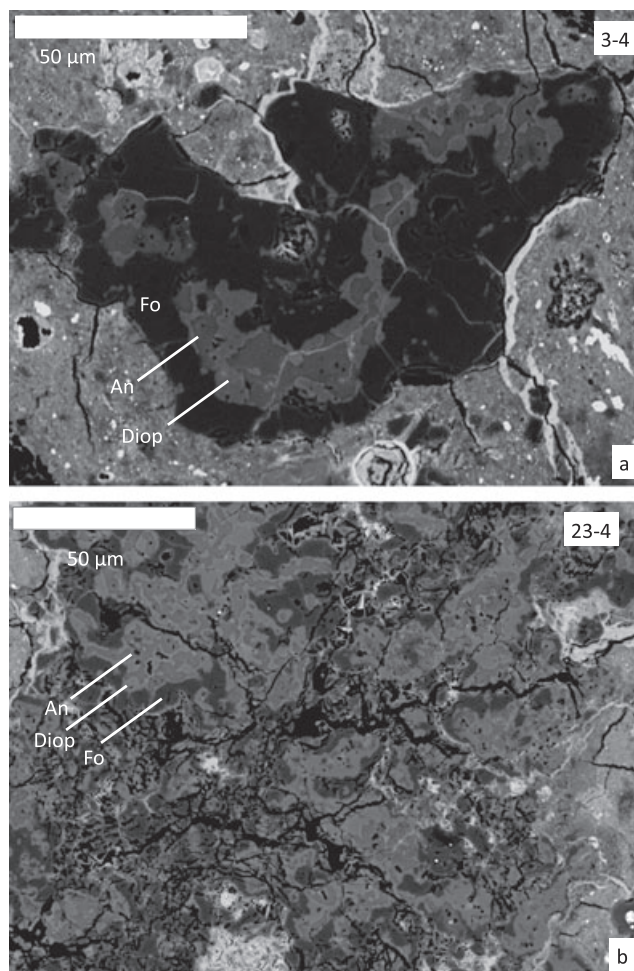

Fig. 7. Backscattered electron images of amoeboid olivine aggregates. a) Inclusion 3-4, with olivine (forsterite) mainly at the rim, enclosing a fine intergrowth of anorthite and Al-diopside. b) Inclusion 23-4, a fine-grained intergrowth of forsterite, anorthite, and Al-diopside. Fo = forsterite; other abbreviations as in previous figures.

from the Wark-Lovering rim sequences (Wark and Lovering 1977; Wark and Boynton 2001) that occur on coarse-grained refractory inclusions, in that Wark-Lovering rims always contain a spinel-rich layer. The Acfer pyroxene rims are similar to those on some inclusions in CR (Weber and Bischoff 1997) and CM chondrites (e.g., Simon et al. 2006), but are more compact than the Al-diopside rims of the "OC" inclusion type described by MacPherson et al. (1983). Unaltered melilite rims are also found on inclusions in CH chondrites (Kimura et al. 1993; Weber and Bischoff 1994).

Mineral Chemistry

Melilite occurs in many of the inclusions. Some representative analyses are given in Table 2. A comparison

Table 2. Representative electron microprobe analyses (wt%) of melilite in refractory inclusions in Acfer 094.

	1	2	3	4	5	6	7
Na_2O	BDL	BDL	BDL	BDL	BDL	BDL	0.03
MgO	1.71	2.13	3.05	1.73	1.03	1.45	1.18
Al_2O_3	32.78	30.63	29.01	32.98	34.97	32.58	33.80
SiO_2	24.18	24.96	25.95	24.37	23.16	23.86	23.22
CaO	41.15	41.31	40.49	40.59	40.93	40.54	41.04
TiO_2	0.06	BDL	BDL	0.05	BDL	BDL	0.18
FeO	0.57	0.61	0.44	0.41	0.41	1.07	0.81
SUM	100.45	99.64	98.94	100.13	100.50	99.51	100.26
Cations per 7 oxygen anions							
Na	0	0	0	0	0	0	0.002
Mg	0.116	0.146	0.210	0.117	0.070	0.100	0.080
Al	1.762	1.662	1.580	1.772	1.874	1.770	1.824
Si	1.102	1.149	1.199	1.111	1.054	1.100	1.063
Ca	2.010	2.038	2.004	1.983	1.995	2.003	2.013
Ti	0.002	0	0	0.002	0	0	0.006
Fe	0.022	0.023	0.017	0.016	0.016	0.041	0.031
Tot	5.014	5.018	5.010	5.001	5.009	5.014	5.019
Åk (mole%)	11.6	14.6	21.0	11.7	7.0	10.0	8.0

Sample numbers and inclusion types: 1: 11-5, Sp+Mel±Pv; 2: 32-6, Sp+Mel±Pv; 3: 49-2, Sp+Mel+Pyx; 4, 5: 59-2, Hib+Gro+Sp+Mel±Pv; 6: 59-6, Hib+Gro+Sp+Mel±Pv; 7: 27-3, Hib±Sp±Pv (mel rim). BDL = below detection limit of 0.021 wt% Na_2O or 0.031 wt% TiO_2.

of the åkermanite contents of melilite in mantles and rims with that in spinel-melilite ± perovskite inclusions is shown in Fig. 8. The melilite in mantles and rims, with average compositions of $Åk_{9.1}$ and $Åk_{8.8}$, respectively, and an overall range of $Åk_{0-23}$ (Fig. 8a), tends to be more gehlenitic than that inside the melilite-rich inclusions, which has a wider range and an average composition of $Åk_{14}$ (Fig. 8b). To see if the mantles or rims are zoned, a total of 15 fine-scale (1 μm point spacing) electron probe traverses were conducted across mantles on four inclusions and across rims on five inclusions. The traverses range from 3 to 15 μm and average 6 μm in length. There is no strongly dominant zoning trend. Among the ten mantle traverses, åkermanite contents increase toward the edge of the inclusion in just two of the cases. They decrease and then increase in three cases, increase then decrease in one sample, and the remainder have two or more reversals. In two of the five rim traverses, åkermanite contents increase toward the edge of the inclusion; in two others they decrease then increase; and in the other one they decrease, increase, and then decrease. Even traverses taken on opposite sides of a nodule can be different from each other.

All melilite is enriched in FeO relative to most of that in CAIs in other meteorites (e.g., Brearley and Jones 1998). As shown in Fig. 9a, melilite in rims and mantles contains at least 0.5 wt% FeO and most of the analyses are between 0.5 and 1.2 wt%. Most of the melilite in the interiors of melilite-rich inclusions (Fig. 9b) also has

significant FeO contents although some are as low as approximately 0.1 wt%. In the interior melilite, there is a slight decrease in the minimum FeO content observed as a function of åkermanite content, whereas in the mantle melilite, the minimum FeO content does not vary with åkermanite content. The lack of correlation between FeO and åkermanite contents in melilite rims and mantles on Acfer inclusions contrasts with mantle melilite of Allende type B1 inclusions (Fig. 9c), in which åkermanite-poor melilite, which occurs at the outermost edges of the inclusions, is the most FeO-rich. In the Acfer 094 rims and mantles, there is no consistent relationship between FeO content and distance from the contact with the matrix. In the 15 traverses mentioned above, one rim is unzoned with respect to FeO and the others exhibit four different trends: six have FeO increasing then decreasing toward the outer edge of the inclusion; four have FeO decreasing then increasing; three have increasing FeO; and one has decreasing FeO contents. Note the order of magnitude difference in FeO contents between Acfer 094 and Allende.

Hibonite in Acfer 094 also has elevated FeO contents relative to most other occurrences (e.g., Brearley and Jones 1998), and a range of TiO_2 contents from 1 to 7 wt%. Representative electron probe analyses are given in Table 3, and data are plotted in Fig. 10. Mg commonly enters hibonite along with Ti^{4+} or Si^{4+} in a coupled substitution for two Al^{3+} cations. Thus, Mg contents are typically strongly correlated with Ti + Si cation abundances, as is seen in Fig. 10a. It is
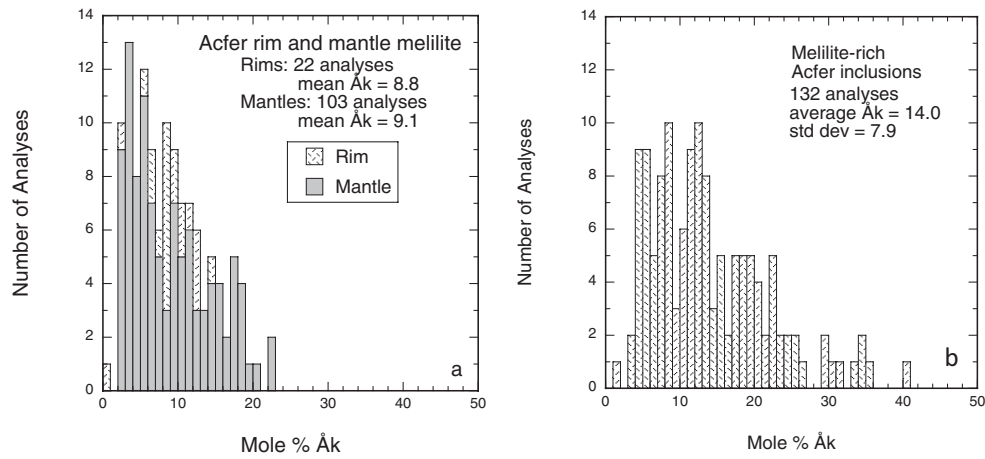
Fig. 8. Histograms of compositions of melilite in rims and mantles (a) and in melilite-rich inclusions (b). The rim and mantle melilite is generally more gehlenitic than melilite in the interiors of inclusions.
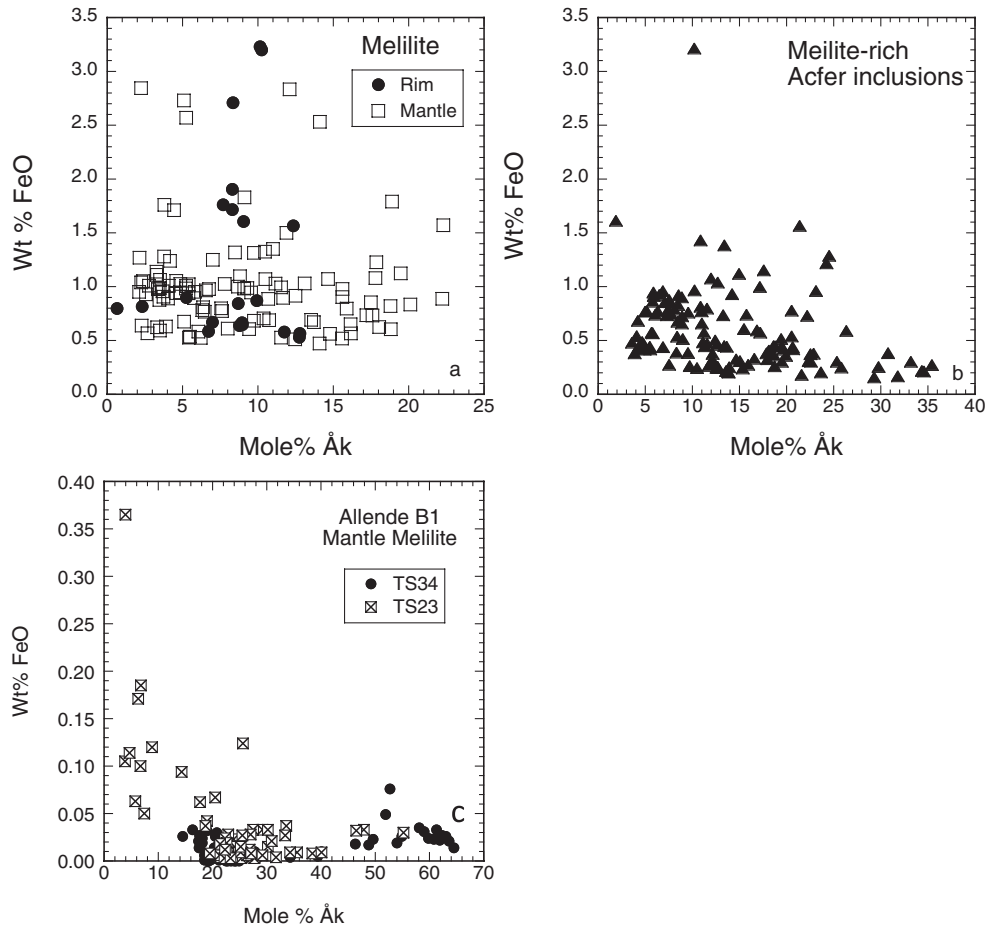

Fig. 9. Plots of FeO contents versus åkermanite contents for melilite from a) rims and mantles on inclusions in Acfer 094; b) in melilite-rich inclusions in Acfer 094; and c) mantles of two type B1 inclusions from Allende. The Acfer data show no correlation between FeO and Åk contents, whereas in the Allende inclusions, the most gehlenitic melilite, which occurs at the edges of the inclusions, is the most FeO-rich.

Table 3. Electron probe analyses of hibonite in Acfer 094 inclusions.

	1	2	3	4	5	6	7	8	9
MgO	3.36	0.78	0.70	0.27	2.76	2.14	2.45	3.71	3.29
Al_2O_3	81.83	89.31	88.85	88.92	82.28	85.07	83.72	79.12	80.53
SiO_2	0.18	0.21	0.03	0.07	0.16	0.10	0.41	0.48	0.19
CaO	8.16	8.43	8.39	8.42	8.64	8.37	8.52	8.69	8.65
TiO_2	5.51	1.43	1.59	1.20	5.27	3.51	4.29	6.39	6.28
V_2O_3	0.58	0.12	0.03	0.04	0.65	0.17	0.09	0.08	0.51
FeO	0.62	0.16	0.60	1.56	0.33	0.81	0.86	0.75	0.37
Sum	100.23	100.45	100.19	100.49	100.09	100.17	100.33	99.22	99.81
Cations per 19 oxygen anions									
Mg	0.567	0.130	0.117	0.045	0.466	0.358	0.411	0.632	0.557
Al	10.912	11.703	11.692	11.720	10.983	11.285	11.104	10.675	10.799
Si	0.020	0.024	0.003	0.008	0.018	0.011	0.046	0.055	0.021
Ca	0.989	1.004	1.004	1.009	1.048	1.010	1.027	1.066	1.055
Ti	0.469	0.119	0.134	0.101	0.449	0.297	0.363	0.550	0.537
V	0.026	0.005	0.001	0.002	0.030	0.008	0.004	0.003	0.023
Fe	0.058	0.015	0.056	0.146	0.031	0.077	0.081	0.072	0.035
Total	13.040	13.000	13.007	13.031	13.025	13.045	13.036	13.054	13.028

Sample numbers: 1: 18-1; 2: ACM4; 3:19-1; 4: L5-1; 5: 59-2; 6: 59-6; 7, 8: 59-3; 9: 27-3.

generally assumed that any Fe found in hibonite has replaced Mg, and plots of Mg + Fe versus Ti + Si cations in hibonite typically yield better 1:1 correlations than plots of Mg versus Ti, supporting this assumption. That is not the case here, however, because the Mg + Fe cation totals tend to plot well above the 1:1 line when plotted against Ti + Si (Fig. 10b). Figures 10c and 10d show why. If Fe were substituting for Mg, a negative correlation between those cation abundances would be expected, and this is not observed (Fig. 10c). Most of the hibonite analyzed has between 0.05 and 0.10 cations of Fe per 19 oxygen anions (approximately 0.4–1.1 wt% FeO) regardless of its Mg content. Exceptions are ACM4, with very low, Murchison-like (MacPherson et al. 1983, 1984; Simon et al. 2006) Fe contents, and L5-1, with very high contents, even for Acfer 094, of 1.1–2.6 wt% FeO. The Mg contents of the unusual hibonite of L5-1 do not correlate with its Ti + Si contents (Fig. 10a); its Fe contents correlate instead (Fig. 10d), and are anticorrelated with Al. As discussed below, it is impossible to find conditions under which FeO-bearing hibonite would form in a nebular setting, and so the Fe contents found here are probably secondary. Calculation of correlation coefficients does not indicate any significant covariation between FeO and the other oxides analyzed, at least partially because most samples have nearly uniform FeO contents, with ranges within samples typically ≤0.2 wt%. In addition, Fe can enter four different crystallographic sites in hibonite (Burns and Burns 1984), and it is possible that secondary Fe, instead of doing so systematically as in L5-1, typically enters various sites in a somewhat

opportunistic, haphazard way, replacing different cations and resulting in an absence of strong correlations.

Except in L5-1 and L5-2 (discussed below), spinel is $MgAl_2O_4$ with 0.1–0.9 wt% V_2O_3, 0.05–1.8 wt% TiO_2, < 0.35 wt% Cr_2O_3, MnO below detection (0.03 wt%) and, like most melilite and hibonite in Acfer 094 inclusions, approximately 0.5–1.2 wt% FeO. Representative electron probe analyses are given in Table 4, and abundances of these oxides in two suites of inclusions are illustrated in Fig. 11. In spinel from spinel + melilite ± perovskite inclusions (Fig. 11a), V_2O_3 contents range from 0.25 to 0.70 wt%, with narrow ranges within inclusions, unlike the wide ranges found by MacPherson and Grossman (1984) in Allende fluffy Type A inclusions. The Acfer 094 samples plotted in Fig. 11a, with V_2O_3 contents typically between 0.30 and 0.55 wt%, also have lower V_2O_3 contents than most Allende fluffy Type As (>1.5 wt%; MacPherson and Grossman 1984) and compact Type As (0.4–1.2 wt%; Simon et al. 1999). Compositions of spinel from hibonite-bearing inclusions overlap with those from analogous inclusions from Murchison on a plot of V_2O_3 versus TiO_2 (Fig. 11b), but not on a plot of Cr_2O_3 versus FeO (Fig. 11c), because of the higher FeO contents of the Acfer spinels. In some inclusions, contents of Cr_2O_3 and FeO are anticorrelated, and in others there is no correlation. Spinel in the Type B-like fragment 23-3 (Fig. 6) has V_2O_3, TiO_2, and FeO contents of 0.15–0.20, 0.2–0.5, and 0.7–1.0 wt%, respectively.

Both L5-1 and L5-2 contain spinel that is much richer in FeO, MnO, and Cr_2O_3 and poorer in V_2O_3 than that in other inclusions. As shown in Fig. 12, FeO
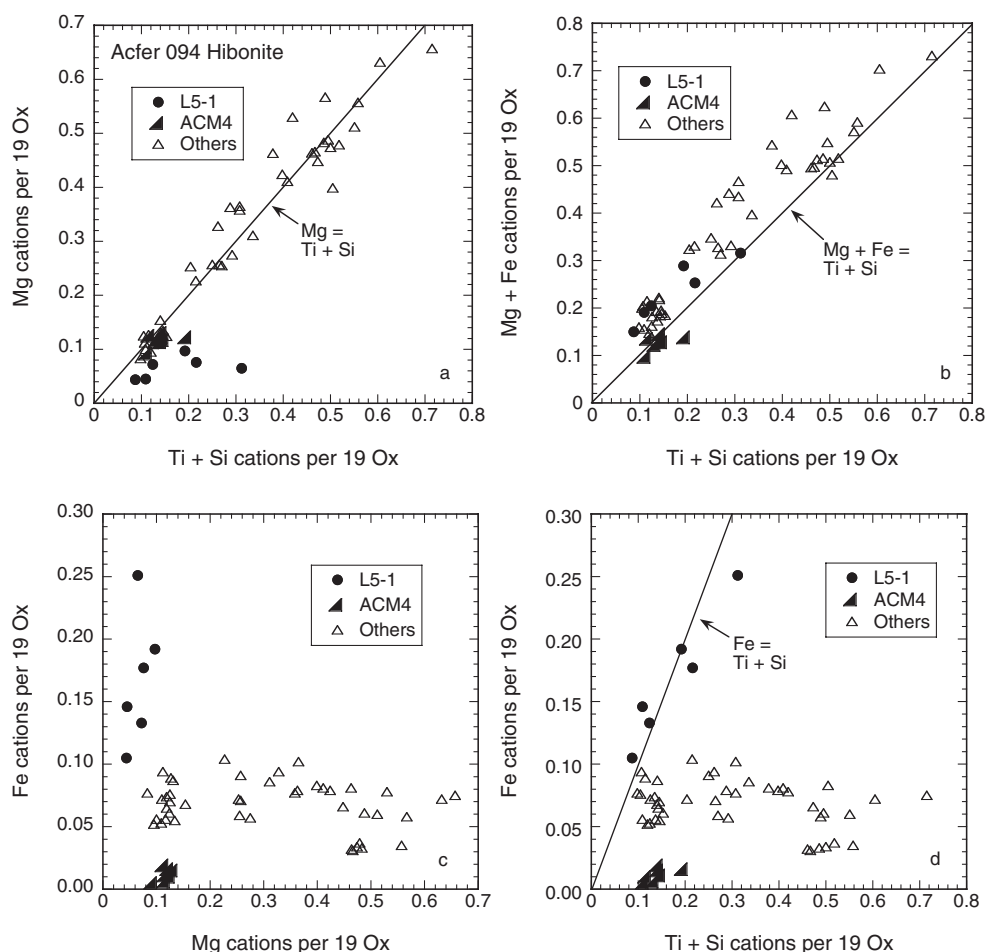
Fig. 10. Analyses of hibonite in Acfer 094 inclusions. a) Mg versus Ti + Si cations per 19 oxygen anions. Most analyses plot on or near the 1:1 reference line, except for those from inclusion L5-1. b) Mg + Fe versus Ti + Si, cations per 19 oxygen anions. Most analyses plot above the 1:1 reference line. c) Fe versus Mg cation contents in hibonite. Fe contents are not correlated with Mg. Most Fe contents fall within a narrow range, except for those from ACM4 (low) and L5-1 (high). d) Fe versus Ti + Si cations per 19 oxygen anions. No correlation is seen except for hibonite in L5-1.

contents are > 10 wt%, and Cr_2O_3 contents are > 2 wt%. MnO contents are approximately 1 wt% except for the Cr_2O_3-rich grain, which has 0.48 wt% MnO. These FeO contents are within the range reported for spinel from CAIs in CO (Russell et al. 1998) and R chondrites (Rout and Bischoff 2008). The spinel in L5-1 and L5-2 has ZnO contents below the detection limit of the electron probe (0.077 wt% ZnO), unlike the R chondrite FeO-rich spinel, which typically contains 1–3 wt% ZnO (Rout and Bischoff 2008).

Most of the pyroxene in Acfer inclusions is aluminous diopside, with a wide range of Al_2O_3 (0.5–21.4 wt%) and Ti contents, occurring in rims on inclusions. Most FeO contents are between 0.4 and 1.0 wt%. Some rims are zoned with Ti and Al contents decreasing from the interiors toward the edges. Like Murchison (Simon et al. 2006), pyroxene in the interiors of Acfer inclusions tends to be Ti- and Al-rich compared

with that in rims. An extreme example is Acfer 094 inclusion 19-3 (Fig. 1e), which has Ti-, Al-rich pyroxene in the interior and a rim of nearly Ti-free aluminous diopside. Compositions of pyroxene from this sample are plotted in Fig. 13. The Ti-rich pyroxene has an average TiO_2^{tot} content of 7.8 wt%, and its average $Ti^{3+}/(Ti^{3+} + Ti^{4+})$ is 0.33.

In contrast, the Type B-like fragment 23-3 contains fassaite with a composition like that found in Allende Type B inclusions. The average of six very similar analyses of fassaite in 23-3 is: MgO, 9.6 wt%; Al_2O_3, 18.1; SiO_2, 39.8; CaO, 24.9; Sc_2O_3, below detection; Ti as TiO_2, 6.4; V_2O_3, 0.14; Cr_2O_3, 0.10; and FeO, 1.2. This gives a $Ti^{3+}/(Ti^{3+} + Ti^{4+})$ ratio of 0.53, corresponding to 3.0 wt% Ti_2O_3 and 3.0 wt% TiO_2. Except for its FeO content, this composition plots on trends defined by Allende fassaite compositions on oxide–oxide plots (e.g., Simon et al. 1991; Simon and Grossman 2006).

Table 4. Representative electron probe analyses (wt%) of spinel in refractory inclusions in Acfer 094.

	1	2	3	4	5	6
MgO	28.63	27.80	28.52	28.64	17.47	16.07
Al_2O_3	70.44	70.84	70.28	70.82	65.70	65.68
SiO_2	0.08	0.02	0.04	0.07	0.08	0.81
CaO	0.21	0.17	0.11	0.06	0.43	0.64
Cr_2O_3	0.10	0.18	0.11	0.23	2.65	3.05
TiO_2	0.23	0.14	0.09	0.40	0.22	0.13
V_2O_3	0.43	0.73	0.14	0.15	BDL	0.05
MnO	na	na	na	BDL	0.90	1.00
FeO	0.45	0.44	0.76	0.98	12.59	13.48
Total	100.57	100.32	100.05	101.35	100.04	100.91
Cations per 4 oxygen anions						
Mg	1.010	0.983	1.012	1.004	0.661	0.605
Al	1.966	1.981	1.972	1.964	1.966	1.955
Si	0.002	0	0.001	0.002	0.002	0.021
Ca	0.005	0.004	0.003	0.002	0.012	0.017
Cr	0.002	0.003	0.002	0.004	0.053	0.061
Ti	0.004	0.002	0.002	0.007	0.004	0.003
V	0.008	0.014	0.003	0.003	0	0.001
Mn	0	0	0	0	0.019	0.021
Fe	0.009	0.009	0.015	0.017	0.267	0.285
Total	3.006	2.996	3.010	3.003	2.984	2.969
Mg/(Mg + Fe)	0.981	0.991	0.985	0.981	0.712	0.680

1: Inclusion 1-1, Sp + Mel; 2: 59-2, Hib + Gro + Sp + Mel + Pv; 3: 59-6, Hib + Gro + Sp + Mel + Pv; 4: 23-3, Sp + Fass; 5: L5-1, Gro + Hib + Sp; 6: L5-2, Cor + Gro + Sp. na = not analyzed; BDL = below the detection limit of the electron probe, 0.03 wt% V_2O_3 or MnO.

The other phases found, grossite, perovskite, and anorthite, all have nearly pure compositions except for FeO contents of approximately 0.5–2 wt%. The corundum that was found is too fine-grained for electron probe analysis. Olivine (in AOAs) is very forsteritic, with compositions between $Fa_{0.5}$ and Fa_2.

DISCUSSION

Comparisons With CAIs in Other Types of Carbonaceous Chondrites

Although the differences between the CAI populations in Acfer 094 and those in the CH, CB, and CR chondrites pointed out by Krot et al. (2004a) are also found in the present work, some of their other contrasts with CAIs in other chondrite types no longer hold true due to findings in the present study. Unlike previous studies of Acfer 094, we found a spinel-hibonite spherule (Fig. 2a); an aggregate of hibonite laths (Fig. 2b); and a relatively coarse, platy hibonite crystal (Fig. 2c), all of which are similar to refractory materials found in CM2 chondrites (e.g., MacPherson et al. 1983; Ireland 1988). Spinel-fassaite inclusion 23-3 (Fig. 6) must be considered a likely fragment of a Type B inclusion, the first reported from Acfer 094. We note that, as in the CH chondrites, grossite-bearing inclusions are not as rare as in most chondrites, and inclusions commonly have melilite rims. Despite these findings, we agree with Krot et al. (2004a) that, of the known chondrite types, the CAI population of Acfer 094 is most similar, but not identical, to that of the CO chondrites. The most common type of inclusion in Acfer 094, small, relatively fine-grained, melilite-dominated inclusions (e.g., Fig. 1a), is also quite common in the CAI populations of CO and CR chondrites (Weber and Bischoff 1997; Russell et al. 1998). In CRs, however, spinel-pyroxene aggregates are more abundant, and hibonite- and grossite-bearing inclusions are rarer, than in Acfer 094 (Weber and Bischoff 1997; Aléon et al. 2002).

Although several of the inclusions from CO chondrites shown in Russell et al. (1998) resemble inclusions in Acfer 094 (melilite enclosing fine spinel; hibonite + spinel enclosed in melilite; hibonite-pyroxene spherules), the populations are not identical, as pointed out by Krot et al. (2004a). Small inclusions consisting of spinel + melilite ± perovskite are found in Acfer 094 and in CM2 chondrites, but the populations are not the same. The inclusions in Acfer 094 are melilite-dominated fragments, whereas most of those in CM2s are spinel-dominated spherules or fragments thereof (Simon et al. 2006), and the two suites have different spinel compositions (Fig. 10). The Acfer inclusions exhibit a unique combination of sizes, textures, mineral
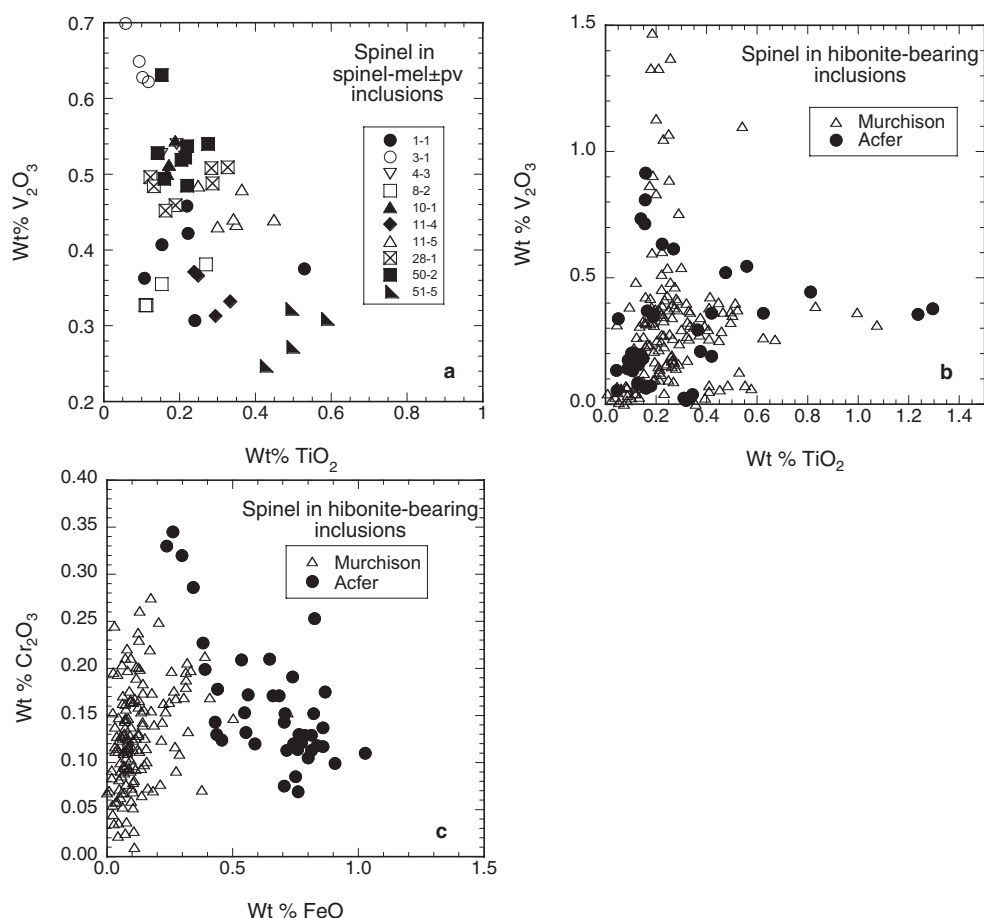
Fig. 11. Minor element contents in spinel in spinel + melilite ± perovskite (SMP), and in hibonite-bearing inclusions from Acfer 094 and from Murchison (Simon et al. 2006). a) wt% V_2O_3 versus TiO_2 in SMP inclusions. b) wt% V_2O_3 versus TiO_2 in hibonite-bearing inclusions. c) wt% Cr_2O_3 versus FeO in hibonite-bearing inclusions.

assemblages, and mineral compositions. Two additional features that help distinguish the Acfer 094 CAI population from those of other chondrites are the melilite rims on many inclusions and the relatively high FeO contents of most of the phases in most of the inclusions. Most CAIs in CO chondrites have rims consisting of diopside and Fe-rich spinel (Russell et al. 1998) rather than melilite. Russell et al. (1998) showed that the FeO contents of melilite and spinel increase with increasing petrologic grade. Inclusions in CO3.0 chondrites, such as ALH 77307 and Colony, have low FeO contents. Unlike inclusions in CO3 chondrites of comparable petrologic grade, those in Acfer 094 have high FeO contents.

Implications for Refractory Inclusion Histories

FeO Contents of Primary Phases in Refractory Inclusions

The matrix of Acfer 094 mainly consists of approximately 40 vol% amorphous silicate, approximately 30% submicron

grains of forsterite (Fa_{0-2}), approximately 20% submicron enstatite (Fs_{0-3}), and approximately 10% other material, with <1% phyllosilicate (Greshake 1997). Amorphous silicate is highly reactive and easily converted to other phases. In Acfer 094, it has excess oxygen relative to that expected for stoichiometric anhydrous oxides (Keller et al. 2009). This is consistent with hydration, which could have caused oxidation of Fe metal, giving the amorphous silicate its observed high FeO contents (Keller et al. 2009). Infrared spectra of Acfer 094 matrix show a water absorption feature (Keller et al. 2009), also consistent with hydration. The extent of hydration was very limited, probably because of low fluid abundances, as the submicron olivine and pyroxene grains enclosed in it were not altered to phyllosilicates. In addition, transmission electron microscopy shows that the sparse serpentine ± chlorite that can be found in the matrix are microcrystallites only nanometers across, an observation that is also consistent with limited, incipient hydration (Greshake 1997).
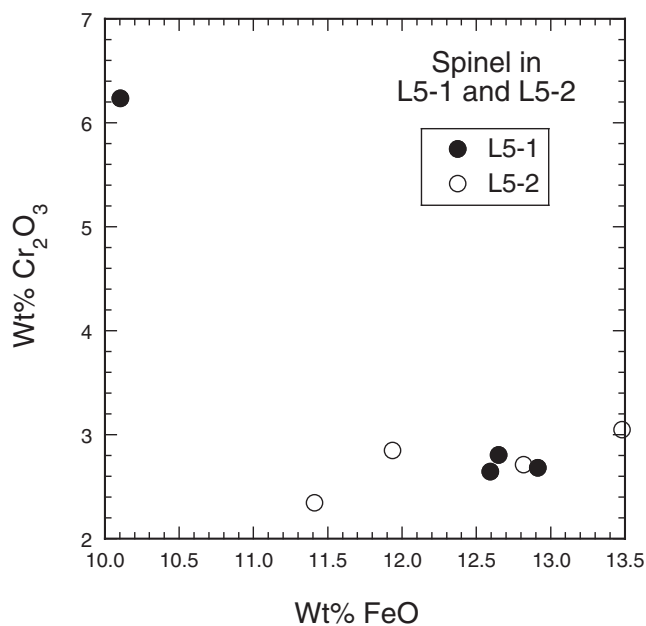
Fig. 12. Plot showing the high Cr_2O_3 and FeO contents of spinel in L5-1 (solid symbols) and L5-2 (open symbols).
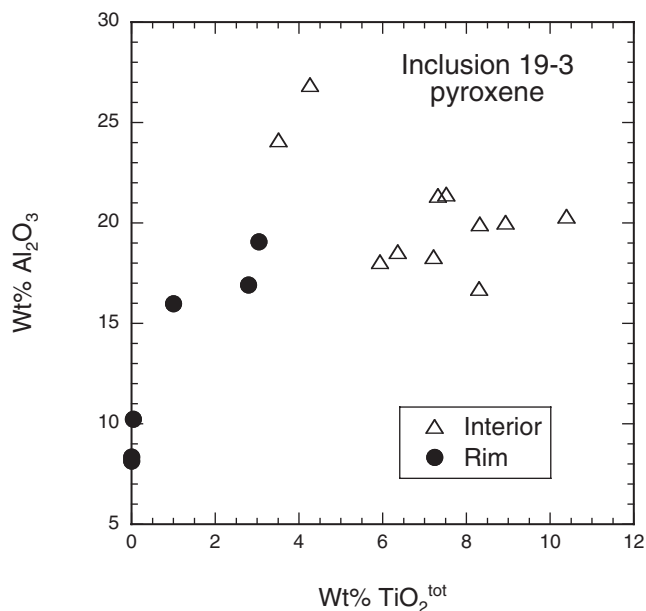

Fig. 13. Plot of Al_2O_3 versus TiO_2^{tot} (all Ti as TiO_2) contents in pyroxene in the spinel-pyroxene inclusion 19-3, shown in Fig. 1e. Both Ti-bearing and Ti-poor (aluminous diopside) pyroxene is present.

Most of the matrix olivine analyzed by Greshake (1997) has < 0.8 wt% FeO. The nearly FeO-free mineral grains are enclosed in FeO-rich (25–30 wt%) amorphous material (Greshake 1997; Keller et al. 2009). Hibonite in Acfer 094 typically contains 0.3–1.1 wt% FeO, and most

melilite has 0.2–2.0 wt% FeO. If all these phases acquired FeO via diffusion from the matrix, we would expect submicron, mafic silicates to have much higher contents than coarser Ca-, Al-rich phases, and this is not observed. Furthermore, as discussed below, hibonite is expected to have much less FeO than coexisting olivine under any circumstances.

Unlike Acfer 094, the CM2 chondrites, such as Murchison, have matrices that are phyllosilicate-rich. The FeO contents of phases in Murchison inclusions can, therefore, be used to estimate how much FeO can be expected to be introduced into CAIs during hydration of the matrix, and they are generally very low (e.g., MacPherson et al. 1983; Brearley and Jones 1998). Even spinel mixed into the matrix from a mechanically disrupted refractory inclusion has only approximately 0.1–0.2 wt% FeO (Armstrong et al. 1982), less than Acfer spinel (Fig. 11c). We conclude that the extensive hydration of CM2 matrices did not lead to FeO enrichment of inclusions in CM2 chondrites, also making it highly unlikely that the limited hydration that the Acfer 094 matrix underwent is related to the elevated FeO contents of the Acfer 094 inclusions.

Although it can be concluded that the FeO contents of Acfer 094 CAIs are preaccretionary, to account for them by equilibrium processes in the solar nebula is impossible. There are no reliable thermodynamic data for FeO-bearing hibonite, grossite, or melilite, but it is likely that these phases are less stable than FeO-bearing olivine and pyroxene at the same conditions. High-temperature condensation of fayalite-bearing olivine from cosmic gases requires oxygen fugacities that are five or six log units higher than those expected in a gas of solar composition, such as may be produced by very large enrichments of dust relative to gas, or of water, compared to solar composition (Grossman et al. 2008). Dust or water enrichments capable of stabilizing hibonite of a given FeO content are probably greater than those necessary for condensing olivine with the same FeO content. High dust or water enrichments, like high total nebular pressures, cause condensation temperatures of all phases to increase, ultimately leading to condensation of liquids, in many cases instead of the phases found in Acfer CAIs. This is a problem especially for systems combining high dust or water enrichments with relatively high nebular pressures. For example, at a pressure of 10^{-3} bar, even a dust enrichment as low as 100×, which stabilizes no more than a few tenths of a mole percent fayalite in olivine at temperatures immediately below those needed for full condensation of Ca and Al, results in a CMAS (CaO-MgO-Al_2O_3-SiO_2) liquid field that takes the place of the stability fields of melilite and calcium aluminates (Ebel and Grossman 2000). On the other hand, at a total pressure of 10^{-6} bar, a dust

enrichment of 800× allows for condensation of many of the phases in Acfer CAIs (corundum, hibonite, grossite, calcium aluminate, perovskite, and spinel, but not melilite) as well as a CMAS liquid, but the olivine that condenses at lower temperature than these phases has so little FeO in it (<0.01 wt%) that the higher-temperature refractory phases would be expected to contain much less FeO than found in the minerals of Acfer 094 CAIs. The situation is not improved when water enrichment is the cause of enhanced oxygen fugacity. At a water enrichment of 700× solar and a total pressure of 10^{-6} bar, corundum, grossite, calcium aluminate, hibonite, melilite, perovskite, and spinel are high-temperature condensates, but the olivine condensing immediately below their condensation temperatures contains only 0.03 mole% fayalite.

The Acfer CAIs consist of phases predicted to condense from a gas of solar composition. They must have acquired their FeO contents after formation in the solar nebula and prior to incorporation in the Acfer parent body. As a nebular setting for the FeO enrichment can be ruled out, we must consider a planetary one, such as an impact vapor plume or a previous parent body. It is possible to envision that a large impact on a water-rich planetesimal, or a collision between two planetesimals, could generate a hot, H_2O-, FeO-rich vapor. Such clouds are relatively short-lived, however, and would be unlikely to persist long enough to cause the pervasive FeO enrichment seen in such a variety of Acfer CAIs.

The most likely setting for the FeO enrichment of the Acfer 094 CAIs, therefore, is in an FeO-rich parent body, prior to incorporation into the Acfer parent body. The nearly uniform FeO enrichment of all phases and the lack of diffusion gradients suggest the inclusions that at least approached equilibration with their surroundings. This implies longer exposure of the CAIs to an FeO-rich environment than could be maintained in a vapor plume. On the other hand, fairly short time scales at high temperatures are also required, otherwise the inclusions would have been recrystallized, and annealed textures are not observed. The reported diffusion coefficient for Fe in gehlenite at 1000 °C is $1.1 \pm 0.8 \times 10^{-14}$ cm^2 s^{-1}, with closure at 800 °C (Morioka et al. 1997). Based on this, the melilite in Acfer inclusions could have equilibrated with respect to FeO in approximately 10^3 yr at 1000 °C. Perhaps, such a time frame would allow diffusion of FeO into melilite and other FeO-enriched refractory phases without recrystallization.

Impacts were common in the early solar system, and most of the Acfer 094 inclusions are fragments. The inclusions could have been liberated from a previous parent body by impact, mixed with "normal" AOAs, chondrules, additional CAIs and amorphous material, and incorporated into the Acfer 094 parent body. Neither AOAs nor chondrules in Acfer 094 are enriched in FeO relative to analogous samples in other meteorites (Brearley and Jones 1998; Krot et al. 2004b). This can simply mean that they were not derived from the FeO-rich parent body envisioned for the CAIs.

Strong evidence for transport of materials from one parent body to another is found in Olsen et al. (1988), who studied four petrographically identified Murchison xenoliths. Three of the objects had been altered in an FeO-rich medium, but one had not. Detailed isotopic and chemical analysis showed that the alteration did not take place in situ, and a well-mixed nebular gas could be ruled out as well. It was concluded that alteration occurred on one or more other parent bodies, prior to accretion onto the Murchison parent body. Those authors also noted that the literature contained over 20 reports of xenoliths in meteorites (their Table 1), suggesting that disruption of planetesimals and reaccretion of materials were important processes in the early solar system. More recently, clasts of many meteorite types have been identified in the Kaidun chondrite breccia (Zolensky and Ivanov 2003; MacPherson et al. 2009).

Melilite Rims and Mantles

Many inclusions in Acfer 094 and CH chondrites (Kimura et al. 1993; Weber and Bischoff 1994) are enclosed in a layer of melilite rather than a sequence of multiple layers of different phases. Most melilite rims are petrographically similar to each other, typically between 5 and 15 μm thick and gehlenitic, with <15 mole% Åk (Fig. 8a). There is no dominant zoning trend and no strong correlation of trends with the mineral assemblage of the host inclusions, though it does appear that, in the rims on spinel-perovskite inclusions, åkermanite contents tend to decrease and then increase with distance from the spinel/melilite contacts at their inner edges. This is the most common zoning pattern found in this study. In addition, several inclusions have melilite rims in which åkermanite contents increase toward the outside of the inclusion, which is normal zoning, assuming growth in that direction, making it unlikely that such rims are solidified melts that crystallized inward. The simplest explanation is that many of the CAIs in Acfer 094 probably encountered a region of the nebula where melilite was condensing.

Interpretation of FeO contents in the rims is also not straightforward. They vary systematically neither with distance from the edges of inclusions nor with åkermanite contents. They do not simply reflect inward diffusion of FeO from the matrix, and therefore may be primary features, reflecting a variety of multistage

thermal histories. If FeO did enter the inclusions by diffusion from the outside inward, it must have been redistributed in heating events prior to accretion.

Four inclusions that do not have melilite rims are petrologically unusual among the Acfer 094 suite. ACM4 (Fig. 2b), the CM2-like hibonite aggregate, has hibonite with the lowest FeO contents found in this study; L5-1 and L5-2 have spinel that is the most FeO-rich found in this study; and 23-3 (Fig. 6) is the first fragment of a Type B inclusion reported from Acfer 094. These unusual inclusions had different sources than most of the Acfer inclusions. They followed different paths to the parent body, and as a result were not exposed to the conditions that led to the formation of melilite rims on typical Acfer inclusions.

Formation of the Most Abundant Types of Inclusions in Acfer 094

As in the present study, Krot et al. (2004a) also found melilite-rich inclusions to be common in Acfer 094. They interpreted many of the ones they found as fluffy Type A (FTA) inclusions, formed by gas-solid condensation. The same can be said for the present suite of inclusions. Many of the melilite-rich inclusions we found are nodules or clusters of nodules that are best classified as FTA inclusions or fragments thereof, somewhat similar to examples shown in MacPherson and Grossman (1984). The melilite-rich inclusions in Acfer 094 tend to contain fine, anhedral spinel grains, like Allende FTAs (MacPherson and Grossman 1984) and unlike the coarse, subhedral to euhedral grains common in igneous compact Type A and Type B inclusions from CV3 chondrites. But, there are also some differences. Electron probe analysis of spinel in Acfer 094 melilite-rich CAIs (Fig. 10a) shows that the present samples do not exhibit the wide ranges of V_2O_3 contents found in FTAs from Allende (MacPherson and Grossman 1984). The present samples, with V_2O_3 contents typically between 0.25 and 0.55 wt%, also have lower V_2O_3 contents than most Allende FTAs (>1.5 wt%; MacPherson and Grossman 1984) and compact Type As (0.4–1.2 wt%; Simon et al. 1999). The melilite-, spinel-rich inclusions in Acfer 094 probably had a different source and/or formed under different conditions than Type A inclusions found in CV3 chondrites.

The silicate-rimmed Sp + Pv and Sp inclusions are also common. The oxide grains are probably condensates upon which silicates, typically melilite followed by aluminous diopside, condensed.

Krot et al. (2004a) reported a continuum in modal mineralogy between melilite-rich and pyroxene-, anorthite-rich CAIs in Acfer 094, and interpreted this observation as an indication that the latter were derived from the former. They also drew a distinction between these inclusions and fragments identified as having igneous textures. Most of the pyroxene-, anorthite inclusions found in the present study may be condensates, as they have the fine, intergrown texture interpreted by Krot et al. (2004a) as having never been molten.

Formation of Grossite-Bearing Inclusions

Grossite-bearing inclusions are relatively rare in most carbonaceous chondrites, and the occurrences reported here can improve our understanding of their formation. Both Grossman et al. (1988) and Kimura et al. (1993) favored an igneous origin for grossite-bearing inclusions in ALH 85085 that they studied, whereas Krot et al. (2004a) favored a condensation origin for most of the grossite-bearing inclusions they found in their study of Acfer 094. Weber and Bischoff (1994) and Weber et al. (1995) provided strong evidence for both condensate and igneous grossite-bearing inclusions. Samples in the present suite also provide evidence that grossite can be found in once-molten inclusions and that it also occurs in inclusions that probably were never molten. Let us consider here whether the data and observations for inclusions 59-2, 59-6, 59-1, L5-,1 and L5-2 are more consistent with an igneous or gas-to-solid condensation origin, or perhaps a combination of these processes.

The first two, 59-2 (Fig. 3d and 3e) and 59-6 (Figs. 3f and 3g), are both compact, rounded inclusions. Both have spinel-hibonite-grossite-perovskite assemblages enclosed in gehlenitic melilite. The spinel is rounded and embayed where it is in contact with melilite, but spinel-hibonite contacts are straight. This texture is reminiscent of the hibonite-bearing Type A inclusions found in Allende by Simon et al. (2001), which contain spinel-hibonite rafts enclosed in melilite, also with straight hibonite-spinel contacts and rounded melilite-spinel contacts. Those authors presented strong evidence that the oxide assemblages are relict and were unstable when enclosed in silicate melts. That possibility must be considered for 59-2 and 59-6 as well. A way to evaluate an igneous versus a condensate origin is to compare the observed phase assemblage and inferred crystallization sequence with those predicted by fractional crystallization and equilibrium condensation models.

The bulk compositions of 59-2 and 59-6, calculated from average phase compositions and their weight proportions, are given in Table 5. They are similar to each other, and for both compositions the liquidus phase is spinel, followed by melilite, grossite, and hibonite (Beckett and Stolper 1994). In both inclusions, however, hibonite is texturally early, before spinel. The texturally inferred crystallization sequence for the inclusions is hibonite, grossite, perovskite, spinel, and melilite. Except

Table 5. Bulk major element contents of grossite-bearing inclusions, obtained by modal recombination.

	59-2	59-6	L5-2
MgO	9.2	11.3	7.3
Al_2O_3	49.5	50.2	56.8
SiO_2	12.2	10.6	0.7
CaO	24.8	22.2	15.6
TiO_2	3.7	4.6	13.6
FeO	0.5	1.1	6.0

for the absence of the very rare phase $CaAl_2O_4$ and the reversal of the order of melilite and spinel appearance, this resembles a portion of the predicted equilibrium condensation sequence for a cooling gas of solar composition at 10^{-3} atm (Grossman 2010). Those calculations predict that grossite should form as a result of reaction between hibonite and gaseous Ca. The serrated contacts between hibonite and grossite in 59-2 and 59-6 could be evidence of this reaction.

Simon et al. (2001) found that the inclusions they studied had isotopically heavy Mg, implying that they had undergone evaporation while at least partially molten. It is not known if either 59-2 or 59-6 have heavy Mg as well, but an interpretation similar to that of Simon et al. (2001) is indicated here. The corroded spinel and adjacent or enclosed grossite, hibonite, and perovskite are probably relict, condensate phases enclosed in later-formed, once-molten melilite. Inclusions 59-2 and 59-6 may be fragments of inclusions similar to the Type A Allende inclusions reported in Simon et al. (2001).

Both Weber and Bischoff (1994) and Krot et al. (2004a) cite irregular shapes and high porosity as evidence for a condensation origin for grossite-bearing inclusions they studied. Among the present samples, inclusion 59-1 (Fig. 3b) is the grossite-bearing inclusion with the highest porosity. It has minor hibonite and grossite, and is dominated by rounded, anhedral spinel grains that have rims of melilite. The rimming of individual grains is most easily explained by reaction between the oxide grains and Ca and Si in the nebular gas, as predicted to occur below 1575 K at a total pressure of 10^{-3} atm (Grossman 2010), prior to agglomeration of them into the inclusion. The preservation of gaps between the grains indicates that the inclusion was not subsequently melted after formation of melilite.

Inclusion L5-1 (Fig. 3c) is an irregularly shaped, loose aggregate of hibonite laths with interstitial grossite and alteration products. Texturally, these features are consistent with formation by gas-solid condensation, but detailed interpretation is not straightforward. Calculations (Ebel and Grossman 2000; Grossman 2010) show that for grossite to form by equilibrium condensation from a gas of solar composition at 10^{-3} atm,

it must do so by reaction of hibonite with gaseous Ca, because approximately 90% of the Al in the system condenses into hibonite prior to grossite formation. In L5-1, the hibonite-grossite contacts are straight and smooth, however, not indicative of a reaction relationship. Perhaps, when L5-1 formed, there was sufficient Al remaining in the vapor that grossite condensed without consuming hibonite. Both the hibonite and spinel in this inclusion record exposure to an oxidizing, FeO-rich environment. The hibonite in this inclusion is unusual in having Fe contents that are correlated with Ti contents (Fig. 10d) and anticorrelated with Al. This suggests that, in this occurrence, Fe extensively replaced Mg, because attempts to define conditions under which Fe-bearing hibonite would form in a nebular setting have not been successful (see above).

Another grossite-bearing inclusion is L5-2 (Fig. 3h). It has an outer shell of spinel that appears to have grown inward, enclosing a grossite-rich core. Based on the bulk composition (Table 5), spinel is the liquidus phase, followed by grossite. This is consistent with the observed textural relationship of these phases, but neither corundum nor hibonite, which are enclosed in grossite, are predicted. If this inclusion formed from a liquid, either the small corundum and hibonite grains are relict, or the bulk composition obtained from the exposed plane is not representative of the inclusion. The interior of this inclusion does consist of an assemblage of phases predicted to condense from a gas of solar composition (Grossman 2010), but they are not predicted to coexist at equilibrium. The smooth alignment of the outer edges of the spinel grains suggests inward growth from a melt-vapor interface, and spinel is the predicted liquidus phase; this makes a molten origin more likely for this inclusion than formation by gas-solid condensation.

Formation of Complex Inclusion 59-3

This inclusion consists of a relatively fine-grained, porous main mass that partially encloses a coarser, more compact clast (Fig. 4). Part of the fine-grained area is spinel-dominated and part is hibonite-dominated (Fig. 4c). During cooling of a gas of solar composition, hibonite is predicted to react with gaseous Ca to form grossite (Grossman 2010), but spinel is known to form directly from hibonite instead, in some cases pseudomorphically replacing it (MacPherson et al. 1984; Simon et al. 2006). The retention of hibonite in 59-3 indicates that only partial replacement of hibonite by spinel occurred, as in Murchison inclusion SH-6 (MacPherson et al. 1984). Hibonite replacement was followed by melilite formation; the hibonite and the spinel grains have melilite rims. Melilite is predicted to
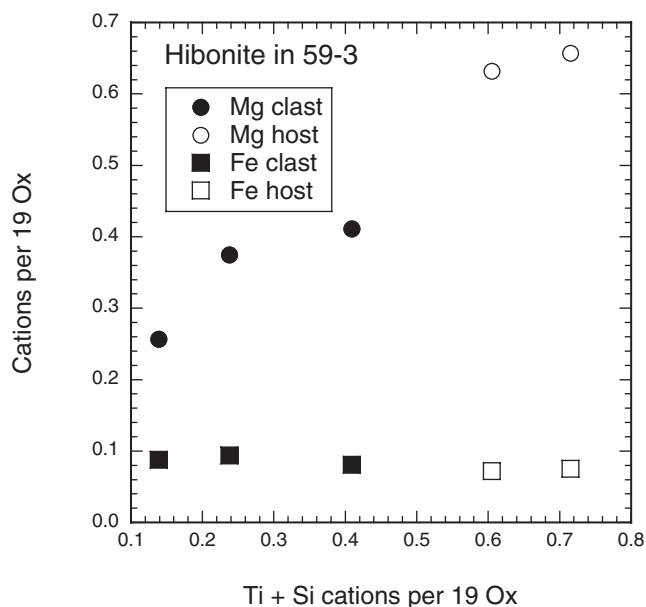
Fig. 14. Compositions of hibonite in the clast and host, inclusion 59-3. Hibonite in the clast is Mg- and Ti-poor compared with that in the host, but they have similar Fe contents.

condense before spinel, but commonly does not, possibly due to unfavorable kinetics relative to formation of spinel from hibonite (Simon et al. 2006). As in 59-1, there are many gaps between the grains, indicating that the inclusion was not subsequently melted after the melilite rims formed.

In addition to the textural differences, the composition of hibonite in the clast is MgO- and TiO$_2$-poor compared with that in the host (Fig. 14), suggesting that they had different origins. Despite these differences, hibonite in the clast has the same Fe content as that in the host (Fig. 14). This implies that Fe was added after incorporation of the clast into the host. As in typical Acfer hibonite, Mg contents correlate with Ti + Si, and Fe contents do not. The coarse, compact texture and curved edge of the clast suggest that it was once molten, in contrast to the porous host. The host and clast are intergrown at the contact, so there may have been some reaction between them when they came into contact with each other, indicating that one or both of the objects was hot at the time.

On the other hand, could the apparent clast/host boundary instead be a reaction front, with the clast a remnant of the primary inclusion and the fine-grained material around it reaction products? This cannot be ruled out, but it seems unlikely. To form the fine-grained hibonite-perovskite-spinel assemblage from the melilite-rich, Ti-poor coarse material would require addition of Ti, to account for the abundance of perovskite and relatively high Ti content of the fine-grained hibonite, and a temperature increase sufficient to vaporize Si, mobilize Ti, and stabilize hibonite, followed by re-formation of melilite upon cooling. It seems more likely that this object contains at least three generations of material, and records the following series of steps in its formation.

First, the clast, a once-molten hibonite-spinel-melilite spherule, formed. Formation of the host inclusion began with condensation of hibonite and partial reaction of the grains with the nebular gas to form spinel. This was followed by further reaction between grains and gas, forming melilite rims on both hibonite and spinel. Melilite is predicted to begin forming prior to spinel (Grossman 2010), but the melilite rims on spinel grains indicate that spinel formed before melilite. The clast could have been incorporated during the gas-grain reactions that formed either spinel or melilite, assuming the clast did not cut off access of the gas to the interior of the inclusion, and prior to deposition of the melilite, anorthite, and diopside rim layers. The clast could have been partially molten when incorporated, which is suggested by the observed intergrowth between host phases and the outer edge of the clast (Fig. 4b). Like most Acfer 094 CAIs, the inclusion was exposed to an FeO-rich planetary fluid, ejected from that body, broken, and then deposited on the Acfer 094 parent body.

Distribution of CAIs in Acfer 094

A comparison of the CAI population found in thin section with that found in the disaggregated material can provide an indication of its variability within Acfer 094, as these materials are from different, probably nonadjacent subsamples. Of the inclusions found in the disaggregated material: 94% have assemblages found in the thin section; three of the four most common assemblages (Sp + Mel ± Pv; Sp + Pv; An + Pyx) are also among the four most common in the thin section; the most common assemblage, An + Pyx, at 20.9% is much more abundant than in thin section (9.7%), whereas the assemblage most common in the thin section, Sp + Mel ± Pv, has similar percentages in the two suites: 22.5% of the CAIs in the section, and 19.4% in the disaggregated material. The proportions of hibonite- and of grossite-bearing inclusions in the disaggregated material, 14% and 9%, respectively, are slightly higher than those seen in thin section in the present study, 13 and 5%, respectively, and not very different from those found by Krot et al. (2004a), who found 10 and 10%. There is no evidence for strong disparities between the CAI populations of different subsamples of Acfer 094.

CONCLUSIONS

1. The Acfer 094 refractory inclusion population is dominated by small, melilite-bearing inclusions, and is somewhat similar to those in CO chondrites, as found in previous studies (Weber 1995; Krot et al. 2004a).

2. Inclusions like those found in CV and CM chondrites are present but are very rare. Abundances of secondary phases are low.

3. Most inclusions have rims of melilite, aluminous diopside, or both. The common occurrence of melilite rims indicates that many Acfer 094 inclusions, including hibonite-bearing ones, encountered a region of the solar nebula, where melilite was condensing.

4. FeO contents seen in primary phases are unusually high. They appear to be preaccretionary, but to account for them in a nebular setting is impossible. Prolonged exposure to an FeO-rich fluid prior to incorporation in the Acfer 094 parent body is required. A previous parent body appears to be the most likely setting.

5. Acfer 094 contains a distinctive population of refractory inclusions. They exhibit a wide variety of mineral assemblages and record different histories from one another.

Editorial Handling—Dr. Adrian Brearley

REFERENCES

Aléon J., Krot A. N., and McKeegan K. D. 2002. Calcium-aluminum-rich inclusions and amoeboid olivine aggregates from the CR carbonaceous chondrites. *Meteoritics & Planetary Science* 37:1729–1755.

Armstrong J. T., Meeker G. P., Huneke J. C., and Wasserburg G. J. 1982. The Blue Angel: I. The mineralogy and petrogenesis of a hibonite inclusion from the Murchison meteorite. *Geochimica et Cosmochimica Acta* 46:575–595.

Beckett J. R. and Stolper E. 1994. The stability of hibonite, melilite and other aluminous phases in silicate melts: Implications for the origin of hibonite-bearing inclusions from carbonaceous chondrites. *Meteoritics* 29:41–65.

Bischoff A., Palme H., Clayton R. N., Mayeda T. K., Grund T., Spettel B., Geiger T, Endreß M., Beckerling W., and Metzler K. 1991. New carbonaceous and type 3 ordinary chondrites from the Sahara Desert (abstract). *Meteoritics* 26:318–319.

Bland P. A., Stadermann F. J., Floss C., Rost D., Vicenzi E. P., Kearsley A. T., and Benedix G. K. 2007. A cornucopia of presolar and early solar system materials at the micrometer size range in primitive chondrite matrix. *Meteoritics & Planetary Science* 42:1417–1427.

Brearley A. J. and Jones R. H. 1998. Chondritic meteorites. In *Planetary materials*, edited by Papike J. J. Chapter 3. Washington, D.C.: Mineralogical Society of America. pp. 3-1–3-398.

Burns R. G. and Burns V. M. 1984. Crystal chemistry of meteoritic hibonites. Proceedings, 15th Lunar and Planetary Science Conference. *Journal of Geophysical Research* 89:C313–C321.

Ebel D. S. and Grossman L. 2000. Condensation in dust-enriched systems. *Geochimica et Cosmochimica Acta* 64:339–366.

Greshake A. 1997. The primitive matrix components of the unique carbonaceous chondrite Acfer 094: A TEM study. *Geochimica et Cosmochimica Acta* 61:437–452.

Grossman L. 2010. Vapor-condensed phase processes in the early solar system. *Meteoritics & Planetary Science* 45:7–20.

Grossman J. N., Rubin A. E., and MacPherson G. J. 1988. ALH85085: A unique volatile-poor carbonaceous chondrite with possible implications for nebular fractionation processes. *Earth and Planetary Science Letters* 91:33–54.

Grossman L., Beckett J. R., Fedkin A. V., Simon S. B., and Ciesla F. J. 2008. Redox conditions in the solar nebula: Observational, experimental, and theoretical constraints. In *Oxygen in the solar system*, edited by MacPherson G. J., Mittlefeldt D. W., Jones J. H., and Simon S. B. Chapter 7. Chantilly, VA: Mineralogical Society of America. pp. 93–140.

Ireland T. R. 1988. Correlated morphological, chemical, and isotopic characteristics of hibonites from the Murchison carbonaceous chondrite. *Geochimica et Cosmochimica Acta* 52:2827–2839.

Keller L. P., Nakamura-Messenger K., and Messenger S. 2009. Amorphous silicates in primitive meteoritic materials: Acfer 094 and IDPs (abstract). *Meteoritics & Planetary Science* 44:A108.

Kimura M., El Goresy A., Palme H., and Zinner E. 1993. Ca-, Al-rich inclusions in the unique chondrite ALH85085: Petrology, chemistry, and isotopic compositions. *Geochimica et Cosmochimica Acta* 57:2329–2359.

Kimura M., Mikouchi T., Suzuki A., Miyahara M., Ohtani E., and El Goresy A. 2009. Kushiroite, $CaAlAlSiO_6$: A new mineral of the pyroxene group from the ALH 85085 CH chondrite, and its genetic significance in refractory inclusions. *American Mineralogist* 94:1479–1482.

Krot A. N., Fagan T. J., Keil K., McKeegan K. D., Sahijpal S., Hutcheon I. D., Petaev M. I., and Yurimoto H. 2004a. Ca, Al-rich inclusions, amoeboid olivine aggregates, and Al-rich chondrules from the unique carbonaceous chondrite Acfer 094: I. Mineralogy and petrology. *Geochimica et Cosmochimica Acta* 68:2167–2184.

Krot A. N., Petaev M. I., Russell S. S., Itoh S., Fagan T. J., Yurimoto H., Chizmadia L., Weisberg M. K., Komatsu M., Ulyanov A. A., and Keil K. 2004b. Amoeboid olivine aggregates and related objects in carbonaceous chondrites:

Records of nebular and asteroid processes. *Chemie der Erde* 64:185–239.

Ma C. 2011. Discovery of meteoritic lakargiite ($CaZrO_3$), a new ultra-refractory mineral from the Acfer 094 carbonaceous chondrite (abstract #5169). *Meteoritics & Planetary Science* 46.

MacPherson G. J. and Grossman L. 1984. "Fluffy" type A Ca-, Al-rich inclusions in the Allende meteorite. *Geochimica et Cosmochimica Acta* 48:29–46.

MacPherson G. J., Bar-Matthews M., Tanaka T., Olsen E., and Grossman L. 1983. Refractory inclusions in the Murchison meteorite. *Geochimica et Cosmochimica Acta* 47:823–839.

MacPherson G. J., Grossman L., Hashimoto A., Bar-Matthews M., and Tanaka T. 1984. Petrographic studies of refractory inclusions from the Murchison meteorite. Proceedings, 15th Lunar and Planetary Science Conference. *Journal of Geophysical Research* 89:C299–C312.

MacPherson G. J., Mittlefehldt D. W., Lipschutz M. E., Clayton R. N., Bullock E. S., Ivanov A. V., Mayeda T. K., and Wang M.-S. 2009. The Kaidun chondrite breccia: Petrology, oxygen isotopes, and trace element abundances. *Geochimica et Cosmochimica Acta* 73:5493–5511.

Morioka M., Kamata Y., and Nagasawa H. 1997. Diffusion in single crystals of melilite: III. Divalent cations in gehlenite. *Geochimica et Cosmochimica Acta* 61:1009–1016.

Newton J., Bischoff A., Arden J. W., Franchi I. A., Geiger T., Greshake A., and Pillinger C. T. 1995. Acfer 094, a uniquely primitive carbonaceous chondrite from the Sahara. *Meteoritics* 30:47–56.

Olsen E. J., Davis A. M., Hutcheon I. D., Clayton R. N., Mayeda T. K., and Grossman L. 1988. Murchison xenoliths. *Geochimica et Cosmochimica Acta* 52:1615–1626.

Pouchou J. L. and Pichoir F. 1984. A new model for quantitative X-ray microanalysis. Part I: Application to the analysis of homogeneous samples. *La Recherche Aerospatiale* 3:13–38.

Rout S. S. and Bischoff A. 2008. Ca, Al-rich inclusions in Rumuruti (R) chondrites. *Meteoritics & Planetary Science* 43:1439–1464.

Russell S. S., Huss G. R., Fahey A. J., Greenwood R. C., Hutchison R., and Wasserburg G. J. 1998. An isotopic and petrologic study of calcium-aluminum-rich inclusions from CO3 meteorites. *Geochimica et Cosmochimica Acta* 62:689–714.

Simon S. B. and Grossman L. 2006. A comparative study of melilite and fassaite in types B1 and B2 refractory inclusions. *Geochimica et Cosmochimica Acta* 70:780–798.

Simon S. B. and Grossman L. 2009. Refractory inclusions in a new section of the unique carbonaceous chondrite Acfer 094 (abstract). *Meteoritics & Planetary Science* 44:A191.

Simon S. B., Grossman L., and Davis A. M. 1991. Fassaite composition trends during crystallization of Allende type B refractory inclusion melts. *Geochimica et Cosmochimica Acta* 55:2635–2655.

Simon S. B., Davis A. M., Grossman L., and Zinner E. K. 1998. Origin of hibonite-pyroxene spherules found in carbonaceous chondrites. *Meteoritics & Planetary Science* 33:411–424.

Simon S. B., Davis A. M., and Grossman L. 1999. Origin of compact type A inclusions from CV3 carbonaceous chondrites. *Geochimica et Cosmochimica Acta* 63:1233–1248.

Simon S. B., Davis A. M., and Grossman L. 2001. Formation of orange hibonite, as inferred from some Allende inclusions. *Meteoritics & Planetary Science* 36:331–350.

Simon S. B., Grossman L., Hutcheon I. D., Phinney D. L., Weber P. K., and Fallon S. J. 2006. Formation of spinel-, hibonite-rich inclusions found in CM2 carbonaceous chondrites. *American Mineralogist* 91:1675–1687.

Vollmer C., Hoppe P., Stadermann F. J., Floss C., and Brenker F. E. 2009. NanoSIMS analysis and Auger electron spectroscopy of silicate and oxide stardust from the carbonaceous chondrite Acfer 094. *Geochimica et Cosmochimica Acta* 73:7127–7149.

Wark D. and Boynton W. V. 2001. The formation of rims on calcium-aluminum-rich inclusions: Step I-Flash heating. *Meteoritics & Planetary Science* 36:1135–1166.

Wark D. A. and Lovering J. F. 1977. Marker events in the early solar system: Evidence from rims on Ca-Al-rich inclusions in carbonaceous chondrites. Proceedings, 8th Lunar Science Conference. pp. 95–112.

Weber D. 1995. Refractory inclusions from the carbonaceous chondrite Acfer 094 (abstract). *Meteoritics* 30:595–596.

Weber D. and Bischoff A. 1994. The occurrence of grossite ($CaAl_4O_7$) in chondrites. *Geochimica et Cosmochimica Acta* 58:3855–3877.

Weber D. and Bischoff A. 1997. Refractory inclusions in the CR chondrite Acfer 059-El Djouf 001: Petrology, chemical composition, and relationship to inclusion populations in other types of carbonaceous chondrites. *Chemie der Erde* 57:1–24.

Weber D., Zinner E., and Bischoff A. 1995. Trace element abundances and magnesium, calcium, and titanium isotopic compositions of grossite-containing inclusions from the carbonaceous chondrite Acfer 182. *Geochimica et Cosmochimica Acta* 59:803–823.

Zolensky M. and Ivanov A. 2003. The Kaidun microbreccia meteorite: A harvest from the inner and outer asteroid belt. *Chemie der Erde* 63:185–246.